

Impact damage in hybrid braided twill composites

G. Zumpano · M. Fox · W. J. Stronge ·
M. P. F. Sutcliffe

Received: 13 June 2008 / Accepted: 14 July 2008 / Published online: 16 August 2008
© Springer Science+Business Media, LLC 2008

Abstract Impact damage to composite plates is significantly reduced by replacing some of the high-strength fibres with more ductile glass or synthetic fibres. Hybrid composites reduce impact damage by distributing more widely the deformations and strain in the contact region. This investigation focussed only on hybrid textile composites with individual tows composed of either carbon or glass which are braided together in a twill textile. At a similar level of impact energy, low and high-speed impact tests resulted in different failure mechanisms dominated, respectively, by quasi-static and flexural wave deformations. The damage severity was evaluated in terms of damage area (C-scan) and absorbed energy.

Introduction

Composite materials are widely used in high-value applications requiring a large ratio of stiffness to weight. In addition to their excellent stiffness-to-weight ratio, composites offer a series of attractive properties including good corrosion resistance and the ability to be formed into complex parts. On the other hand composite materials are susceptible to impact damage caused by the brittle nature of the reinforcing fibres, limited interlaminar shear strength and a lack of reinforcement in the thickness direction [1].

Impact damage tends to be located internally in the form of delamination of plies and matrix cracks that show little visual evidence of damage.

In general there are at least two phases of impact damage in composites: (1) dynamic compaction of the composite plate which is being compressed ahead of any colliding missile; and (2) delamination of plies in the neighbourhood of the impact site [2]. The exact nature of damage will depend on the composite weave architecture, resin properties and the properties of the colliding missile [1, 3]. However, for low-speed impact, damage modes that are observed are bending damage on the distal surface and an approximately circular internal delamination, followed by fibre splitting and perforation or shear failure at high incident energies [4]. Moreover, the impact damage tends to initiate on the distal surface if the ratio of plate thickness to projectile nose radius is <1 (i.e. thin plates) and on the impact surface if the plate thickness is greater than the projectile nose radius (thick plates) [3, 5]. High-speed impacts trigger different failure mechanisms because the deformation field induced by the impact induces higher frequency modes in addition to the fundamental (quasi-static) mode of deformation [6].

Impact damage results in a reduction of the composite in-plane compressive strength mainly due to delamination [1]. Delamination between plies occurs in the interlaminar (resin rich) regions where the extensional and bending stiffness differs due mainly to different fibre orientations between the layers or, in some cases, different materials [6, 7]. Further investigations have suggested that delamination is initiated by matrix cracks in both opening and shear modes [8, 9].

Tougher resins or three-dimensional woven composites can be used to increase the delamination toughness and so improve the composite impact resistance. With tougher

G. Zumpano · W. J. Stronge (✉) · M. P. F. Sutcliffe
Engineering Department, Cambridge University, Trumpington
Street, Cambridge CB2 1PZ, UK
e-mail: wjs@eng.cam.ac.uk

M. Fox
School of Materials, Manchester University, Paper Science
Building, Sackville Street, Manchester M60 1QD, UK

matrices and stronger interfaces, larger impact energies are required to initiate delamination [10]. Through thickness tows in three-dimensional weaves act as crack stoppers by altering the fracture paths from intra-tow mode to inter-ply mode; this approximately doubles the fracture toughness [11].

An alternative way to reduce the impact damage is to tackle the brittle nature of high-strength fibres, which have small ultimate strains. Some carbon fibres can be replaced by ductile glass fibres in order to increase the strain to failure. This results in trading off stiffness in order to achieve larger ultimate strains and strengths [12], and so potentially smaller areas of damage [13]. These mixtures are called hybrid composites and can be classified as: hybrid lay up (one material per ply); hybrid textile (one material per tow/yarn); and commingled composites (hybrid tow/yarn).

In this paper, the results of low and high-speed impacts on a hybrid textile (hybrid ply/layer composites) are presented. First, the hybrid composite will be introduced and the experimental impact procedure explained. Then, experimental data are analysed (C-scan damage area; absorbed (dissipated) energy; contact force; and sample surface micrographs) in order to understand the failure mechanisms triggered by impact.

Materials

The material under investigation was a hybrid textile with an overall fibre volume fraction of 51%, of which 75% was high strength carbon fibres and the remaining 25% glass fibres. The carbon and glass fibres were braided from separated tows in 2×2 twill dry preforms (Fig. 1). These were laid up in four layers with epoxy resin injected by resin transfer moulding, to produce $40 \times 40 \text{ cm}^2$ plates with a nominal thickness of 4.5 mm. Finally, in order to investigate possible size effects on impact generated damage, square specimens of two sizes 20×20 and $13 \times 13 \text{ cm}^2$ were cut from two $40 \times 40 \text{ cm}^2$ plates using a diamond saw.

The effects of colliding mass and speed were investigated by impacting the plates with different masses and impact energies as described in Table 1.

Low-speed impacts (2–6 m/s) were carried out using the Cambridge drop tower (DT, Fig. 2), fitted with an impactor of mass 0.754 kg. The impactor had a 12.5-mm hemispherical head made of steel. The speed of the impactor was measured just prior to impact by timing the passage of the impactor between two infrared cells placed 5 cm apart. Impact and rebound speeds were also measured from images taken from a high-speed camera. A force transducer behind the impactor head was employed to measure the contact force during impact.

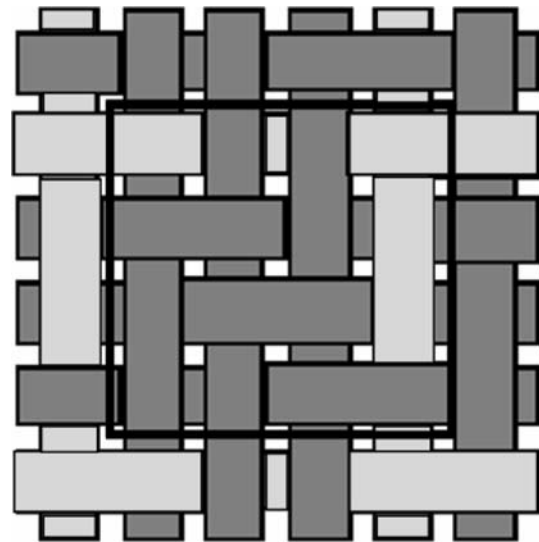


Fig. 1 2×2 twill unit cell geometry (the light-shaded tows are glass fibres)

Table 1 Table of experiments

Number of tests	Plate size (cm)	Mass (g)	Device	Impact energy (J)
2	13×13	754	DT	13, 23
5	13×13	12.5	GG	12, 25, 32, 39, 48
2	20×20	21.5	GG	25, 48
4	13×13	21.5	GG	28, 33, 41, 52

High-speed impacts (44–88 m/s) were carried out using a gas gun (GG, Fig. 3) with 12.5-mm diameter hemispherical-nosed steel projectiles that had masses of 12.5 and 21.5 g. The projectile impact speed was estimated by a pair of infrared cells spaced 5 cm apart that were positioned at the end of the GG. Impact and rebound speeds were measured from high-speed camera images.

For both the DT and the GG, the speed taken from the infrared cells slightly underestimated the impact speed because of further acceleration between the measurement point and the specimen. Therefore, these speed measurements were used only for calibration purposes and the speeds reported were taken from the high-speed camera images. A maximum difference of 5% between the speed estimated by the infrared cells and the high-speed camera was observed.

The procedure used for the impact experiments was as follows:

1. Pre-impact C-scan.
2. Perform impact test.
3. Post-impact C-scan.
4. High-speed camera post-processing: impact and rebound speeds.
5. Surface micrography of impacted samples.

Fig. 2 Cambridge DT with enlarged view of impactor head and force transducer

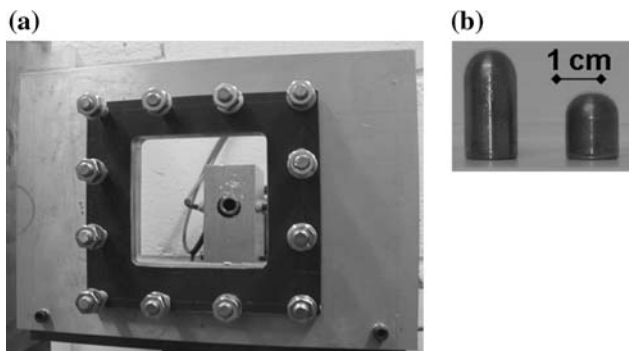
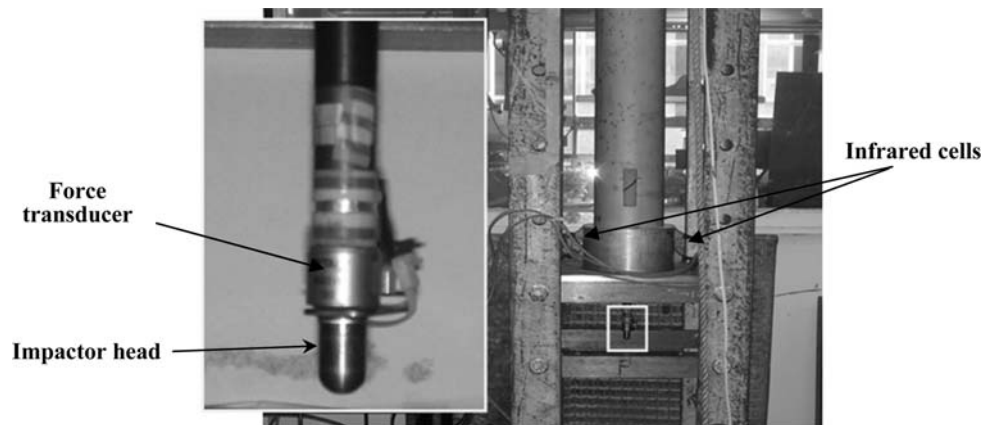


Fig. 3 Photographs of (a) GG muzzle viewed through specimen clamping device and (b) hemispherical-nosed high-speed projectiles

Results

Response mode

Before showing results from DT and GG impacts, it is useful to consider the three main types of dynamic responses of composite plates [14]. The first is dominated by dilatational waves travelling through the plate thickness. In this case, the contact time is comparable with the through thickness travelling time of dilatational waves. The second type of response is dominated by flexural waves emanating from the impact site. For this type of plate response, the contact times are smaller than the travelling time of flexural waves from the impact centre to the closest plate boundary. For contact times longer than that required for the waves to reach the boundary, the plate undergoes quasi-static deformation in the fundamental mode (third type plate response).

A mass criterion [14] was proposed by Olsson to classify the type of composite plate response to impact. This criterion states that for a projectile of mass M striking the centre of a composite plate of mass M_p :

- $\frac{M}{M_p} \leq \frac{1}{\pi\sqrt{2}} \cong 0.25 \rightarrow$ Flexural wave dominated dynamic response.

- $\frac{M}{M_p} \geq 2 \rightarrow$ Quasi-static response.
- $0.25 \leq \frac{M}{M_p} \leq 2 \rightarrow$ Complex response.

For the impactors and composite plates employed in the present investigation, conditions can thus be characterised as follows:

- DT $M/M_p = 6.4$, therefore the plate dynamics is anticipated as type 3, a quasi-static response.
- GG, $M/M_p = 0.11$ and 0.19 , for the 12.5 and 21.5 g projectiles, respectively. Hence, the plate dynamics is dominated by flexural waves.

Consequently, different types of dynamic response are predicted for the DT and GG impacts experiments.

Absorbed energy and damage severity

A high-speed framing camera was used to estimate both the impact and rebound speeds. The projectile location in high-speed images was measured to an accuracy of 1.2 mm for the GG and 0.6 mm for the DT. In order to reduce the error in the estimates of the impact and rebound speeds, the change in position was evaluated over ten frames, to obtain an accuracy for projectile speed of ± 0.3 m/s for the DT (4.5 kHz sampling frequency) and ± 2 m/s for the GG (18 kHz sampling frequency). Once the impact and the rebound speeds were evaluated, the absorbed energy was estimated as the difference between the kinetic energies at impact and rebound (note that this absorbed energy is the sum of the fracture energy and energy associated with residual elastic vibrations).

Figure 4 shows the absorbed energy for all the tests undertaken, showing that the absorbed energy increases almost linearly with increasing impact energy. In addition, the energy absorbed during low-speed impacts (circles) was about 40% smaller than that due to high-speed impacts (squares) at comparable impact energies. The level of absorbed energy for the high speed, 12.5 g projectile impacts (squares), was always larger than that for the 21.5 g

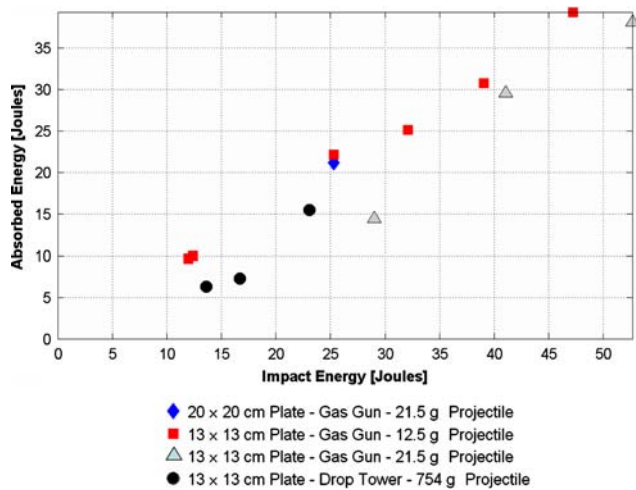


Fig. 4 Absorbed energy

projectile (triangles). However, data scatter and possible errors in the accuracy of the absorbed energy suggest that the difference in mass between these two projectiles does not significantly affect the absorbed energy.

Figure 5 plots the variation of C-scan damage area with impact energy. The measurement of C-scan damage area increases linearly with increasing impact energy, mirroring the increase in absorbed energy as shown in Fig. 4. For similar impact energies, the DT damage area was observed to be 20–30% smaller than the GG high-speed damage area. Consistently, impact by the 12.5 g projectile resulted in a slightly larger damage area than impacts by the 21.5 g projectile. In general, there was no recognisable difference in damage between the 13 and 20 cm plates when struck by either of the high-speed projectiles, at comparable impact energies. The damage areas for the 12.5 g projectile striking at 25 J and the 21.5 g projectile striking at 52 J are noticeably smaller than the trend. This difference is a result

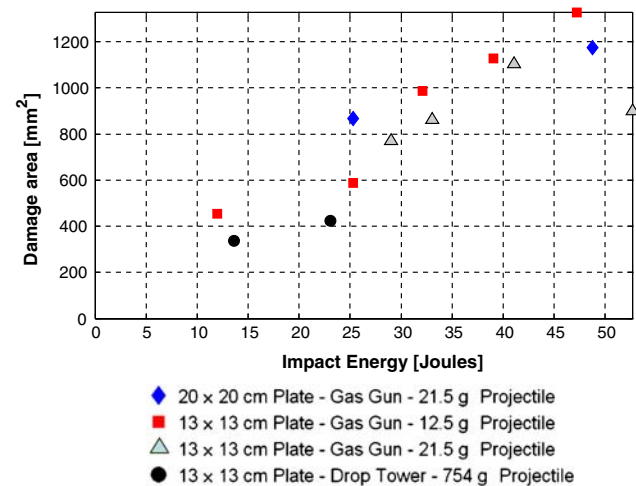


Fig. 5 C-scan damage area

of the projectile striking on and breaking a glass fibre tow and thereby limiting the ability of this tow to transmit damage to adjacent carbon fibre tows.

Surface micrography

In order to identify and compare the failure mechanisms involved in low and high-speed impacts we aim to correlate experimental data about absorbed energy and damage area with surface micrographs of the damages surfaces. In this section, the glass fibre and carbon fibre tow locations are correlated to micrographs of surface fractures to allow identification of different types of fracture. In subsequent photos of the damage surface, the impact centre is identified as a light blue circle, while the glass and carbon tows are identified by yellow and red rectangles, respectively.

Low-speed impacts

DT impact samples showed a clearly identifiable dent on the impact surface with tow splitting and fibre breakage cracks emerging from its rim (see Figs. 6a and 7a); the number and length of these surface fractures increased with increasing impact energy. On the distal surface of plates hit with 13 J impact energy, only glass fibre debonding was observed (Fig. 6c). However, when the impact energy was increased to 23 J, fibre breakage, tow splitting and inter-tow cracks were observed on the impact surface (Fig. 7c), in addition to a fracture emerging from the periphery of the dent.

The tow cracks seen on the impact surface propagate outwards from the outer rim of the dent suggesting that the dent formed first and that, once this had formed, subsequent damage in the form of tow splitting and inter-tow cracks developed at the edge of the dent. The dent is formed when the contact stresses underneath the impactor cause matrix-dominated failure. A further increase in contact force can result in an increasing area of delamination damage around the dent rim, eventually leading to tow failures in the form of tow and fibre splitting. This picture of a two-stage damage process is supported by the contact force histories reported in Fig. 8. There is a large drop in contact force after a peak of about 3 kN (interestingly occurring at similar times and loads for the 12 and 23 J impact energies), presumably due to the loss of stiffness associated with the denting damage mechanism (and any associated delamination). The subsequent re-loading history shows a correspondingly reduced stiffness. There are subsequent drops in contact force (e.g. for the 23 J impact at a load of around 6.3 kN, see Fig. 8), which are presumed to be due to tow failure in the form of tow and fibre splitting. These failure mechanisms are associated with a sharper drop of contact force and a larger decrease in the gradient of the contact force due to the large amount of energy dissipated

Fig. 6 Impact sample micrographs: impact surface (a) DT (13 J, 6 m/s); (b) GG (12 J, 43 m/s); distal surface (c) DT (13 J, 6 m/s); (d) GG (12 J, 43 m/s). Red and yellow rectangles locate the carbon and glass tows, respectively

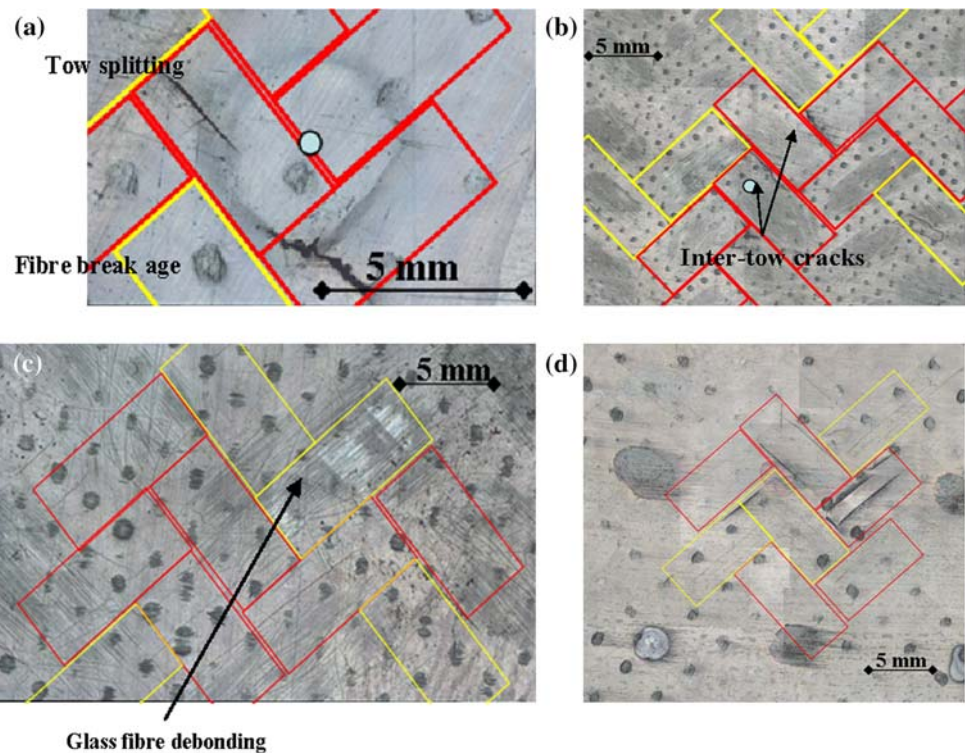
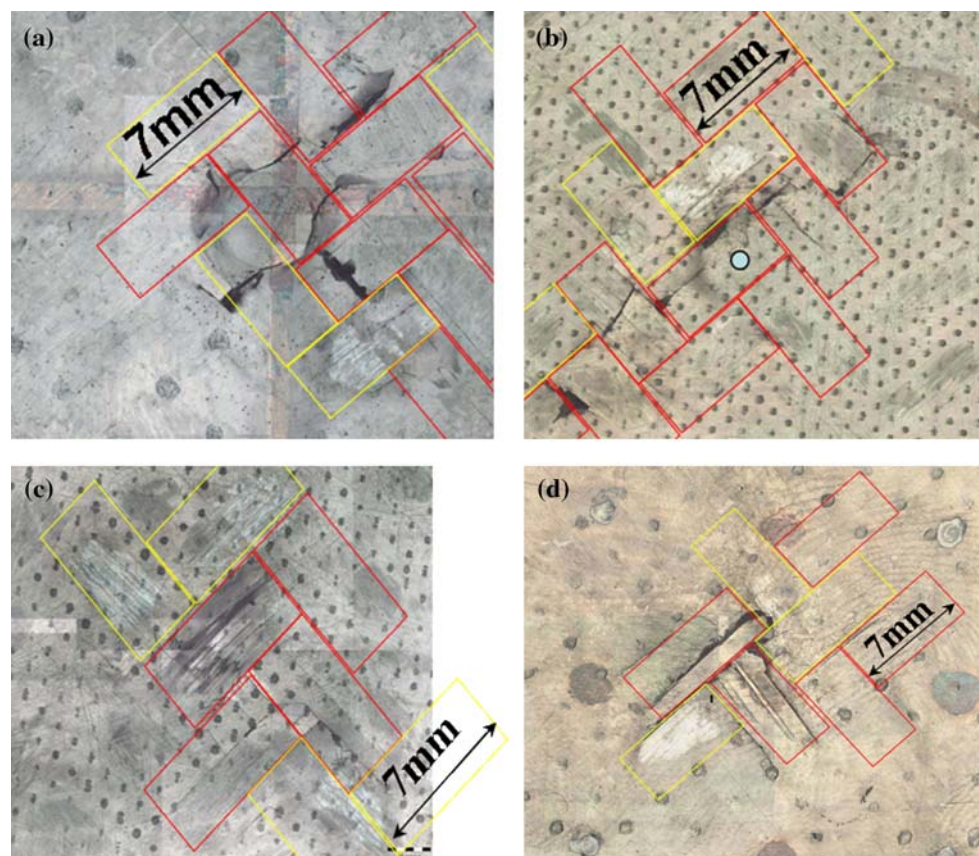


Fig. 7 Impact sample micrographs: impact surface (a) DT (23 J, 7 m/s); (b) GG (25 J, 60 m/s); distal surface (c) DT (23 J, 7 m/s); (d) GG (25 J, 60 m/s)



by the tow failure [15]. Similar contact force behaviour was observed during low-speed impact experiments on E-glass epoxy laminates [16]. It is also interesting to note that the

lower energy 12 J impact has a significantly smoother force profile. Presumably the waviness in the force signal is associated with fracture development around the contact

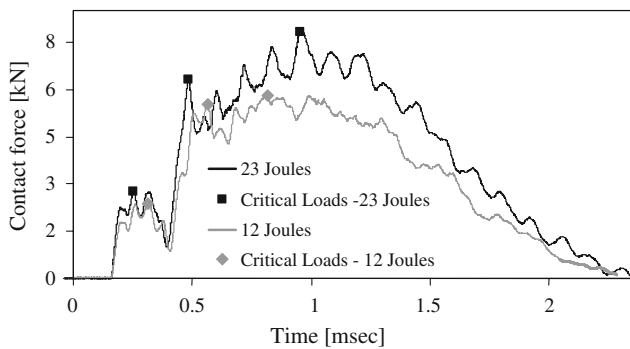


Fig. 8 Contact force time history, DT experiments

area. Further modelling work is needed to confirm this picture of damage progression.

High-speed impacts

Surface micrography of specimens subject to high-speed impact reveal similar failure modes to those observed for low-speed impact, i.e. fibre and tow splitting, inter-tow cracks and glass fibre debonding. However, for impact energies below 15 J the high-speed impacts caused no observable dent whereas at a similar impact level the low-speed impact left an obvious dent. Also, for high speeds there were no cracks emerging from the edge of the contact region (compare Fig. 6a, b for low and high-speed impacts, respectively, where the circles identify the impact centre). Moreover, on the distal surface (Fig. 6d), a bulge could be observed with inter-tow as well as tow and fibre splitting cracks. In contrast, the low-speed impact showed no apparent cracking but there was glass fibre debonding. With an increase of impact energy above 15 J a dent started forming on the impact surface, though this was still shallower than the dents seen for the low-speed impacts at corresponding impact energies. Cracks (tow and fibre splitting and inter-tow cracks) were clearly propagating along preferential $\pm 45^\circ$ tow directions. It was observed that damage was more extensive along the glass fibre tow

that was located closest to the impact centre (Figs. 7a, b and 12a). This highly loaded glass fibre tow transfers its load to neighbouring carbon fibre tows. However, since the carbon tows have a lower strain to failure of 1.7–1.8% compared with 4.5% for the glass tows, the carbon tends to fracture before the glass. An effect of this force transfer mechanism along individual tows can be seen on the modest ellipticity of the delamination areas as shown in Figs. 9–12b, where the major axis of the ellipse lies along the preferential damage propagation direction. Although, this failure mechanism gives rise to a large energy dissipation due to failure of carbon tows, it tends to increase the delamination area. Finally, when a glass fibre tow is struck directly and the tow breaks, this preferential damage mechanism along the tow path no longer takes place and the delamination area in that direction decreases. Glass tow breakage was identified in section “Absorbed energy and damage severity” as being responsible for some unusually low values of damage area as shown in Fig. 5.

This behaviour highlighted a dependence of the plate dynamic response on the local stiffness distribution around the impact point; this variation depends on weave architecture and material properties. During high-speed impact the plate dynamics include higher modes of deformation that represent a flexural wave travelling outward from the impact site. In contrast, low-speed impact results in a quasi-static or fundamental mode of deformation. Consequently, at any level of impact energy, high-speed impact yields larger radial curvature on the plate in a region around the impact point. This leads to larger surface stresses and consequently to more surface damage, in comparison with low-speed impact at the same energy level [14, 17], as confirmed by Fig. 5. This explains why the specimen plates were sufficiently large that no size effects were observed.

High and low-speed impacts failure mode comparison

As predicted by the mass criterion, the low and high-speed impacts highlighted two different failures modes. Low-

Fig. 9 12.5 g projectile impact (39 J, 79 m/s): (a) impact surface micrograph; (b) C-scan

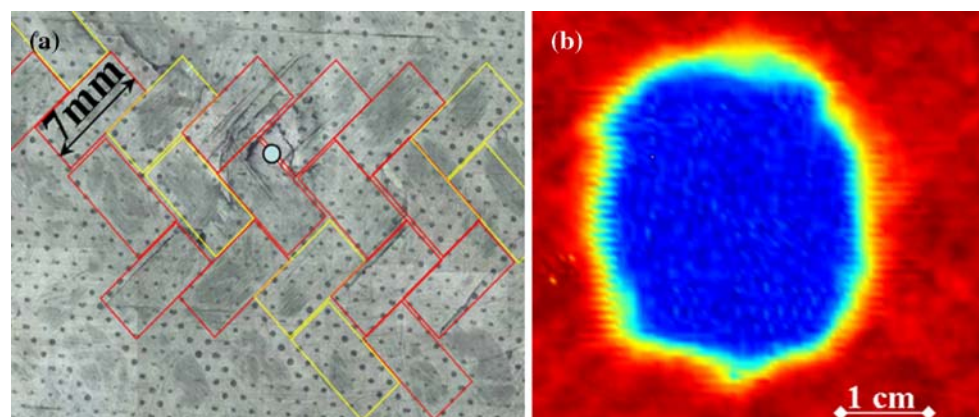


Fig. 10 21.5 g projectile impact (33 J, 56 m/s): (a) impact surface micrograph; (b) C-scan

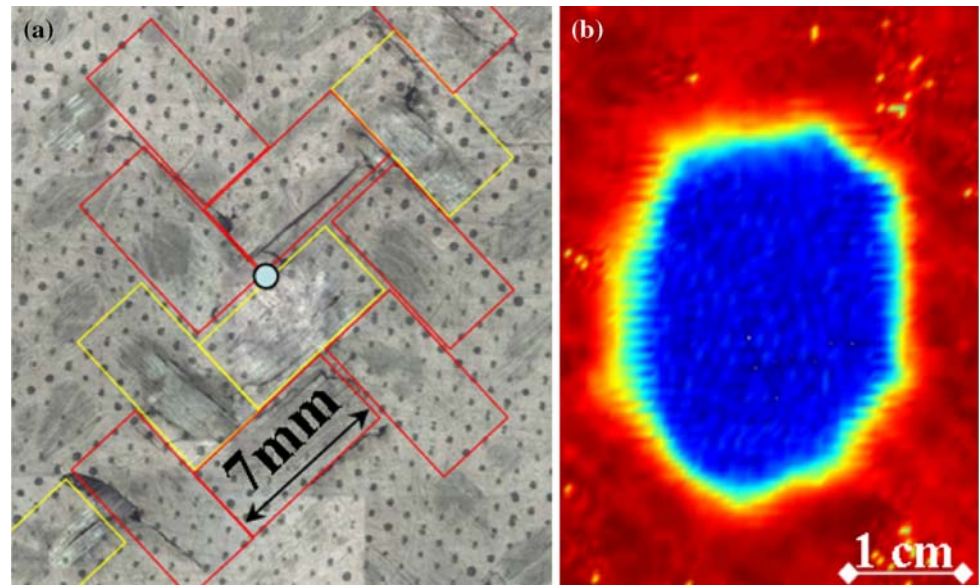


Fig. 11 21.5 g projectile impact (52 J, 69 m/s): (a) impact surface micrograph; (b) C-scan

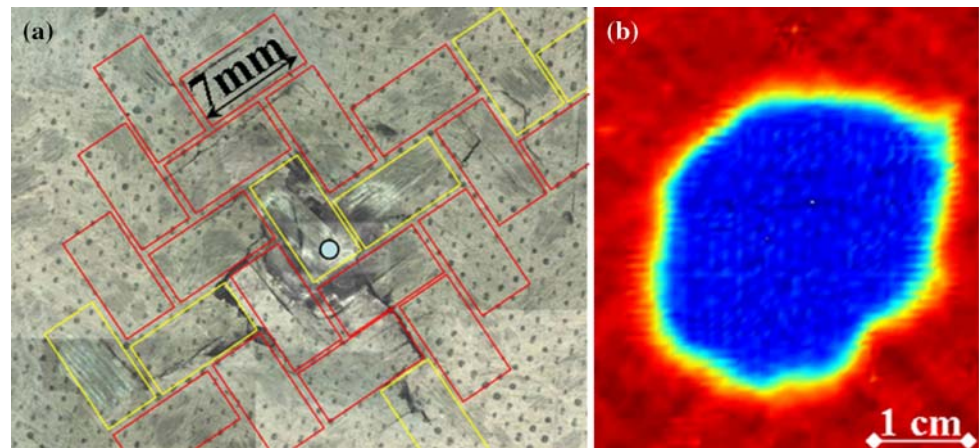
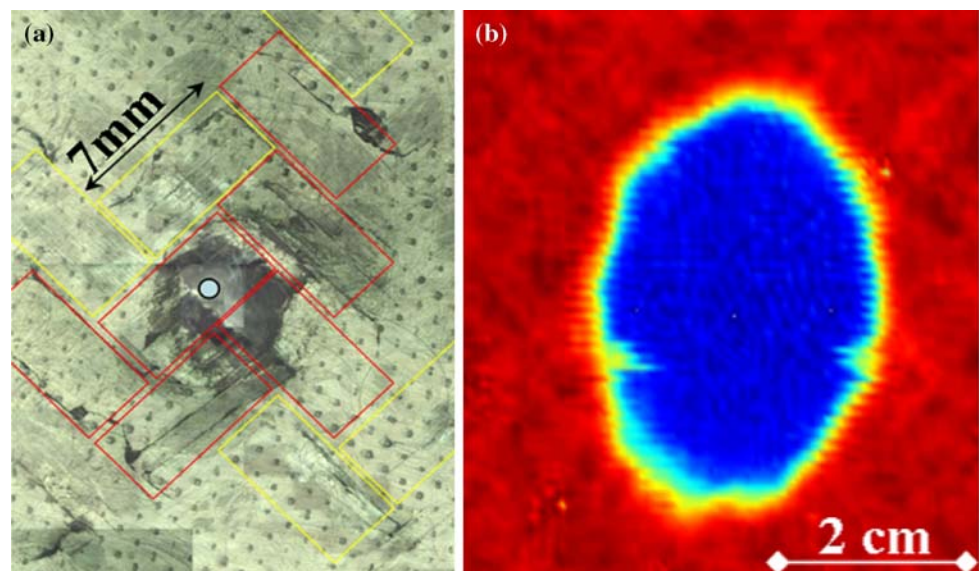


Fig. 12 21.5 g projectile impact on large plate (48 J, 68 m/s): (a) impact surface micrograph; (b) C-scan



speed impact resulted in a quasi-static response of the plate that led to the formation of a dent, delamination (detected by C-scan) and tow failures propagating outwards from the outer rim of the dent. In contrast, high-speed impact resulted in plate dynamics that were dominated by flexural waves, which in turn led to damage propagating according to the distribution of local stiffness. For equal impact energies, high-speed impact resulted in a larger damage area, as shown in Fig. 5.

Conclusions

In this investigation, experimental evidence of fibre breakage, tow splitting and delamination from low and high-speed impacts on braided hybrid textile composites was analysed. Low and high-speed impacts resulted in different patterns of failure mechanisms as a consequence of quasi-static and flexural dynamic modes of deformation, respectively.

Low-speed impacts were observed to be not significantly affected by the textile composite architecture, in agreement with literature observations. On the other hand, high-speed impact resulted in a rather unique damage evolution, dominated by the textile architecture and its hybrid nature. Damage was observed to propagate along a preferential direction dictated by glass tows adjacent to the point of impact.

For both low and high-speed impacts, the impact energy was the main factor affecting the density of damage.

Acknowledgements Contributions are gratefully acknowledged from the Engineering and Physical Sciences Research Council (grant

EP/C538145/1), University of Nottingham, Cranfield University, Rolls-Royce Group plc., Dowty Propellers (Part of GE's Aviation Business), Carr Reinforcements Ltd and JR Technology Ltd.

References

1. Tarim N, Findik F, Uzun H (2002) *Compos Struct* 56:13. doi: [10.1016/S0263-8223\(01\)00177-5](https://doi.org/10.1016/S0263-8223(01)00177-5)
2. Mouritz AP (2001) *Composites Part B* 32:431. doi: [10.1016/S1359-8368\(01\)00015-4](https://doi.org/10.1016/S1359-8368(01)00015-4)
3. Matemilola SA, Stronge WJ (1995) *Compos Eng* 5:211
4. Sutherland LS, Guedes Soares C (1999) *Compos Sci Technol* 59: 2243
5. Cantwell WJ, Morton J (1990) *Compos Sci Technol* 38:119. doi: [10.1016/0266-3538\(90\)90002-M](https://doi.org/10.1016/0266-3538(90)90002-M)
6. Bahei-El-Din YA, Zikry MA (2003) *Compos Sci Technol* 63(7):923. doi: [10.1016/S0266-3538\(03\)00021-6](https://doi.org/10.1016/S0266-3538(03)00021-6)
7. Kuboki T, Jar P-YB, Forest TW (2003) *Compos Sci Technol* 63:943. doi: [10.1016/S0266-3538\(02\)00316-0](https://doi.org/10.1016/S0266-3538(02)00316-0)
8. Finn SR, Springer GS (1993) *Compos Struct* 23:177. doi: [10.1016/0263-8223\(93\)90221-B](https://doi.org/10.1016/0263-8223(93)90221-B)
9. Liu S, Kutlu Z, Chang F-K (1993) *J Compos Mater* 27(5):436. doi: [10.1177/002199839302700501](https://doi.org/10.1177/002199839302700501)
10. Thanomsilp C, Hogg PJ (2003) *Compos Sci Technol* 63:467
11. Ebeling T, Hiltner A, Baer E, Fraser IM, Orton ML (1997) *J Compos Mater* 31:1318
12. Naik NK, Ramasimha R, Arya H, Prabhu SV, Shama Rao N (2001) *Composites Part B* 32:565. doi: [10.1016/S1359-8368\(01\)00036-1](https://doi.org/10.1016/S1359-8368(01)00036-1)
13. Dutra RCL, Soares BG, Campos EA, Silva JLG (2000) *Polymer (Guildf)* 41:3841. doi: [10.1016/S0032-3861\(99\)00552-2](https://doi.org/10.1016/S0032-3861(99)00552-2)
14. Olsson R (2000) *Composites Part A* 31:879. doi: [10.1016/S1359-835X\(00\)00020-8](https://doi.org/10.1016/S1359-835X(00)00020-8)
15. Wu E, Chang LC (1998) *J Compos Mater* 32:702
16. Aslan Z, Karakuzu R, Okutan B (2003) *Compos Struct* 59:119. doi: [10.1016/S0263-8223\(02\)00185-X](https://doi.org/10.1016/S0263-8223(02)00185-X)
17. Corum JM, Battiste RL, Ruggles-Wrenn MB (2003) *Compos Sci Technol* 63:755. doi: [10.1016/S0266-3538\(02\)00265-8](https://doi.org/10.1016/S0266-3538(02)00265-8)